

Dirac Magnons in a Honeycomb Lattice Quantum XY Magnet CoTiO_3 Bo Yuan¹,¹ Ilia Khait,¹ Guo-Jiun Shu,^{2,3} F. C. Chou⁴, M. B. Stone⁵, J. P. Clancy⁶,
Arun Paramekanti,¹ and Young-June Kim¹¹*Department of Physics, University of Toronto, Toronto, Ontario, M5S 1A7, Canada*²*Department of Materials and Mineral Resources Engineering, National Taipei University of Technology, Taipei 10608, Taiwan*³*Institute of Mineral Resources Engineering, National Taipei University of Technology, Taipei 10608, Taiwan*⁴*Center for Condensed Matter Sciences, National Taiwan University, Taipei, 10617 Taiwan*⁵*Neutron Scattering Division, Oak Ridge National Laboratory, Oak Ridge, Tennessee 37831, USA*⁶*Department of Physics and Astronomy, McMaster University, Hamilton, Ontario L8S 4M1 Canada*

(Received 2 July 2019; revised manuscript received 13 January 2020; accepted 31 January 2020; published 12 March 2020)

The discovery of massless Dirac electrons in graphene and topological Dirac-Weyl materials has prompted a broad search for bosonic analogues of such Dirac particles. Recent experiments have found evidence for Dirac magnons above an Ising-like ferromagnetic ground state in a two-dimensional (2D) kagome lattice magnet and in the van der Waals layered honeycomb crystal CrI_3 , and in a 3D Heisenberg magnet Cu_3TeO_6 . Here, we report our inelastic neutron scattering investigation on a large single crystal of a stacked honeycomb lattice magnet CoTiO_3 , which is part of a broad family of ilmenite materials. The magnetically ordered ground state of CoTiO_3 features ferromagnetic layers of Co^{2+} , stacked antiferromagnetically along the c axis. The magnon dispersion relation is described very well with a simple magnetic Hamiltonian with strong easy-plane exchange anisotropy. Importantly, a magnon Dirac cone is found along the edge of the 3D Brillouin zone. Our results establish CoTiO_3 as a model pseudospin-1/2 material to study interacting Dirac bosons in a 3D quantum XY magnet.

DOI: [10.1103/PhysRevX.10.011062](https://doi.org/10.1103/PhysRevX.10.011062)

Subject Areas: Condensed Matter Physics

I. INTRODUCTION

The discoveries of graphene and topological insulators have led to significant advances in our understanding of the properties of electrons in solids described by the Dirac equation. In particular, the fruitful analogy between fundamental massless Weyl-Dirac fermions in nature and electrons in graphene or topological semimetals has allowed physicists to simulate theories of particle physics using tabletop experiments [1–6]. Remarkably, the concept of Dirac particles is not limited to electrons or other fermionic quasiparticles, prompting a search for analogues in bosonic systems, such as photonic crystals [7,8], acoustic metamaterials [9], phonons in noncentrosymmetric crystals [10,11], and magnons in quantum magnets [12–15]. In particular, Dirac magnons, or more broadly defined topological magnons [16–21], have attracted much attention as platforms to investigate the effect of interparticle interaction or external perturbations

on Dirac bosons, and they are of potential interest in spintronic applications.

In contrast to light and sound, the symmetry-broken states and emergent bosonic excitations of quantum magnets depend crucially on dimensionality and spin symmetry, which provides a fertile playground for examining the physics of topological bosons. To date, gapped topological magnons in Ising-like ferromagnets have been reported in a kagome lattice material $\text{Cu}(1,3\text{-bdc})$ [18] and in a layered honeycomb magnet CrI_3 [19]. On the other hand, magnons exhibiting symmetry-protected band crossings have been found only in a single material, a three-dimensional (3D) Heisenberg antiferromagnet Cu_3TeO_6 [20,22]. It is thus desirable to explore new test beds with distinct spin symmetries to expand our understanding of the physics of Dirac magnons.

In this paper, we propose that CoTiO_3 with a simple ilmenite structure is a new candidate for realizing a Dirac magnon in a 3D quantum XY magnet. The magnetic lattice of Co^{2+} ions in CoTiO_3 is a stacked honeycomb lattice, exactly the same as in ABC stacked graphene. Below $T_N = 38$ K, this material exhibits magnetic order with ferromagnetic planes stacked antiferromagnetically along the c axis. Our inelastic neutron scattering (INS) experiments reveal crystal field excitations and sharp low-energy

Published by the American Physical Society under the terms of the [Creative Commons Attribution 4.0 International license](https://creativecommons.org/licenses/by/4.0/). Further distribution of this work must maintain attribution to the author(s) and the published article's title, journal citation, and DOI.

dispersive spin waves. Although Co^{2+} is a spin $S = 3/2$ ion, resulting in a large magnetic signal, our analysis of the observed low-energy crystal field levels provides evidence for strong, easy-plane, single-ion anisotropy leading to a pseudospin $\tilde{S} = \frac{1}{2}$ doublet ground state. The low-energy spin wave reveals magnon modes crossing along a Dirac nodal line (DNL) of the 3D Brillouin zone (BZ), near which the magnon dispersion takes the form of a Dirac cone. In contrast with earlier examples of Ising-like and Heisenberg magnets, a simple model with dominant nearest-neighbor XY ferromagnetic (FM) exchange and antiferromagnetic interlayer second-neighbor exchange provides a good description of the magnon dispersion in CoTiO_3 .

Unlike all other topological magnon candidates, large, pristine, single-crystal samples of this material, suitable for neutron scattering and other experiments, can be grown using the conventional floating zone method. The availability of large single crystals enables one to systematically investigate the impact of doping and external perturbations—pressure, strain, or magnetic field—on Dirac magnons, which has been extensively studied for Dirac fermions in graphene [23–29]. Moreover, we find that simple DNL geometry in CoTiO_3 gives rise to surface states only on particular surfaces. Large single crystals that can be cut along different surfaces thus also offer the unique potential for a direct observation of the surface magnons in this material.

II. CRYSTAL STRUCTURE, CRYSTAL FIELD LEVELS

As shown in Fig. 1(a), CoTiO_3 crystallizes in an ilmenite structure ($R\bar{3}$) that consists of alternating layers of edge-sharing CoO_6 or TiO_6 octahedra [30]. Details of the synthesis (and other experimental details) are provided

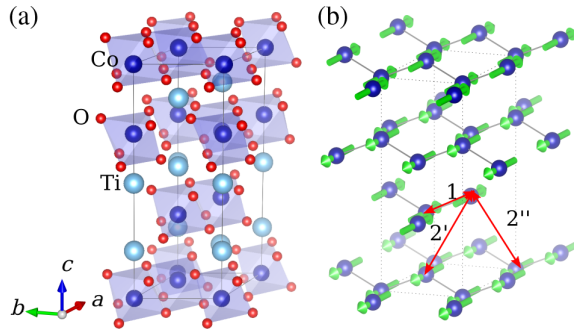


FIG. 1. (a) Structure of CoTiO_3 . A nonprimitive hexagonal unit cell, which is used to describe our data, is indicated by solid black lines. (b) Magnetic structure of the Co^{2+} sublattice. The Co^{2+} magnetic moments (shown by green arrows) order ferromagnetically within each honeycomb plane and antiferromagnetically along the c axis. Red arrows labeled 1, 2', and 2'' are the magnetic couplings considered in the spin-wave calculation.

in the Supplemental Material [31]. The magnetic properties of CoTiO_3 are determined by the Co^{2+} ions that reside in slightly buckled honeycomb layers; see Fig. 1(b). These layers are ABC stacked along the c direction, with neighboring honeycomb planes displaced diagonally by a third of the unit cell.

Atomically, each Co^{2+} in a high spin state is surrounded by a trigonally distorted oxygen environment, which is depicted in the inset of Fig. 2(b). Local electronic states in Co^{2+} are determined by a combination of trigonal distortion Δ_{trig} and spin-orbit coupling λ . To elucidate the magnetic ground state of each Co^{2+} ion, we measure the crystal field excitations using high-energy inelastic neutron

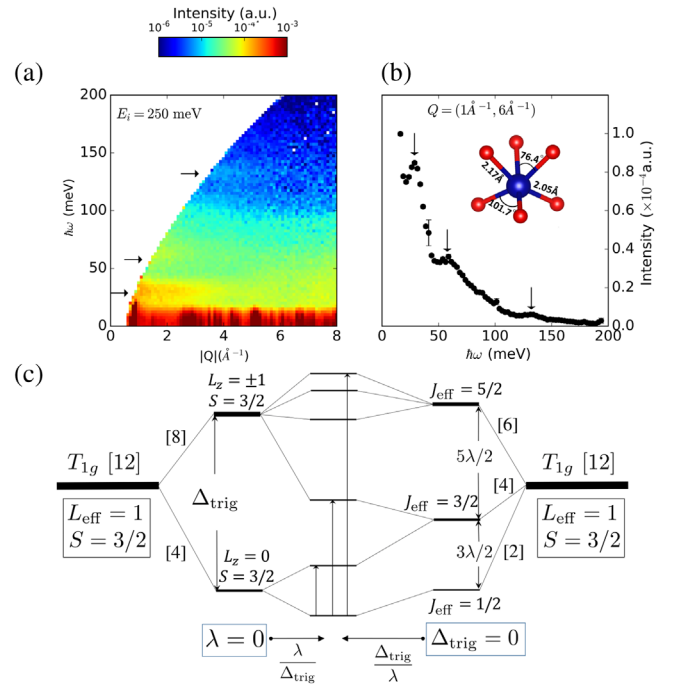


FIG. 2. (a) Neutron scattering intensity plot on a log scale as a function of energy (in meV) and momentum transfer (in \AA^{-1}) for an incident neutron energy of $E_i = 250$ meV. The data were collected at $T = 5$ K. Since there is no directional dependence of the crystal field excitations, the scattering intensity is averaged over all orientations, and only the magnitude of momentum transfer is shown. (b) Momentum integrated intensity for $1.0 \text{ \AA}^{-1} < |\mathbf{Q}| < 6.0 \text{ \AA}^{-1}$ plotted as a function of energy transfer. The inset shows trigonally distorted oxygen octahedra around each Co^{2+} ion. Horizontal and vertical arrows in panels (a) and (b), respectively, mark the positions of observed crystal field excitations. (c) Schematic crystal field levels for Co^{2+} (three t_{2g} holes, with total $L_{\text{eff}} = 1$ and $S = 3/2$) in the regimes $\lambda \ll \Delta_{\text{trig}}$ (left) and $\Delta_{\text{trig}} \ll \lambda$ (right), where λ is the SOC and Δ_{trig} is the trigonal distortion. Vertical arrows correspond to the sharp transitions seen in panels (a) and (b). The numbers in the square brackets denote degeneracies of the states. (See Supplemental Material [31] for a further description of the figure.)

scattering (INS). The results shown in Figs. 2(a) and 2(b) clearly reveal three transitions at 29(2) meV, 58 (7) meV, and 132(3) meV, together with a broad continuum between 60 meV and 120 meV. Their intensities decrease with increasing momentum transfers as shown in Fig. 2(a), which confirms their magnetic origin.

We model the crystal field levels using a single-ion Hamiltonian $H_{\text{ion}} = \lambda \vec{L} \cdot \vec{S} + \Delta_{\text{trig}} L_z^2$, where Hund's coupling favors total spin $S = 3/2$ and total orbital angular momentum $L_{\text{eff}} = 1$, and $\hat{z} \parallel \mathbf{c}$. We find that $\lambda = 28(1)$ meV and $\Delta_{\text{trig}} = 45(6)$ meV provide a good description of the observed crystal field transitions (see Supplemental Material [31] for details), leading to transitions at (29, 59, 110, 119, 132) meV. The obtained value of λ is in good agreement with previously reported values for other cobaltates [32,33]. The full electronic-level diagram of a single Co^{2+} ion determined using these parameters is shown in Fig. 2(c). The three sharp transitions observed in Figs. 2(a) and 2(b) are indicated by vertical arrows; the other two expected transitions could not be identified unambiguously in the data but seem to be buried in the broad continuum intensity.

When $\Delta_{\text{trig}} \gg \lambda$, the orbital angular momentum is quenched, $L_z = 0$, leading to a pure spin $S = 3/2$ moment. The excited states at an energy Δ_{trig} have $L_z = \pm 1$ as shown in the $\Delta_{\text{trig}} \gg \lambda$ limit of the crystal field levels in Fig. 2(c). SOC splits this $S = \frac{3}{2}$ quartet via an effective single-ion term $H_{\text{ion}}^{\text{eff}} = \Delta S_z^2$ with $\Delta > 0$, leading to a ground doublet with $S_z = \pm 1/2$. In the opposite regime, $\Delta_{\text{trig}} \ll \lambda$, SOC will lead to a ground $J_{\text{eff}} = 1/2$ doublet and excited $J_{\text{eff}} = 3/2, 5/2$ levels [34,35]. Weak Δ_{trig} splits the excited levels and mixes different J_{eff} wave functions. With increasing Δ_{trig} , the ground $J_{\text{eff}} = 1/2$ doublet smoothly connects with the $S_z = \pm 1/2$ doublet in the first scenario. Magnetic properties of CoTiO_3 are determined by the ground-state doublet, which acts like an $\tilde{S} = 1/2$ pseudospin. For the fitted values of $(\lambda, \Delta_{\text{trig}})$, the ratio between g factors parallel (g_{\parallel}) and perpendicular (g_{\perp}) to the honeycomb plane is $g_{\parallel}/g_{\perp} \approx 1.6$ for the pseudospin, leading to a large anisotropy proportional to $(g_{\parallel}/g_{\perp})^2$ in the magnetic susceptibility, qualitatively consistent with the experiment in Ref. [36] (see also Supplemental Material [31]). Upon projection to the ground-state doublet, even a simple Heisenberg model for the original $S = 3/2$ spins leads to a strong easy-plane exchange anisotropy between effective low-energy $\tilde{S} = 1/2$ pseudospins.

III. ORDERED STATE AND MAGNON DISPERSION

Below the Neel temperature $T_N = 38$ K, Co^{2+} magnetic moments confined within the \mathbf{ab} plane are ordered ferromagnetically within each honeycomb layer and

antiferromagnetically along the \mathbf{c} direction, giving rise to the ordered structure shown in Fig. 1(b) [30]. Energy- and momentum-resolved magnon spectra of CoTiO_3 are obtained by inelastic neutron scattering with an incident energy, $E_i = 50$ meV. In Fig. 3, we show magnon spectra along $(H, -H)$ [Figs. 3(a) and 3(b)] and (H, H) [Figs. 3(c) and 3(d)], which lie within the honeycomb plane at fixed $L = 0.5$ as well as along L at $(1, 1, L)$ [Fig. 3(e)]. The directions of these momentum transfers are denoted by thick blue lines in the 2D reciprocal space map in Fig. 3(l). Strongly dispersive magnon modes extending up to about 12 meV are observed in all directions, which indicates the presence of significant intraplane and interplane couplings in CoTiO_3 . The magnetic Bragg peaks are located at $(1, 0, 0.5)$ in Fig. 3(a) and $(1, 1, \pm 1.5)$ in Fig. 3(e) and are consistent with earlier neutron diffraction results [30]. Acoustic magnon modes are found to emanate from these Bragg peaks.

Our data show linear crossings of magnon bands at Dirac points whose positions in reciprocal space are marked with circles in Fig. 3(l). These Dirac crossings occur at an energy $\hbar\omega^* \sim 8.5$ meV, as highlighted by the arrows in Figs. 3(b) and 3(c). The linear dispersions of magnon modes away from these points are well resolved in our data. Figures 4(a)–4(c) show a more detailed view of the magnon dispersion relation around the Dirac point, depicted by a red circle with a solid line in Fig. 3(l), along three different directions: (I) $(\xi - \frac{1}{3}, \frac{2}{3})$, (II) $(\eta - \frac{1}{3}, \eta + \frac{2}{3})$, and (III) $(2e - \frac{1}{3}, -e + \frac{2}{3})$. These momentum space slices all pass through \mathbf{K}' as shown in Fig. 4(d). From Figs. 4(a)–4(c), the magnon dispersions are found to cross at \mathbf{K}' along all three directions. To show this more clearly, intensity versus energy plots at different fixed momenta are shown in Figs. 4(e)–4(g) (the plots at different momenta have been vertically offset for clarity). For instance, in Fig. 4(e), all cuts except at $\xi = 0$ show two peaks corresponding to the two magnon branches in Fig. 4(a). On the other hand, only a single peak is visible at $\xi = 0$, suggesting the presence of a magnon crossing within instrumental resolution. Similar magnon crossing behavior is shown in Figs. 4(f) and 4(g). Figure 4(d) schematically illustrates that having the magnon mode crossing at a *single* point \mathbf{K}' along *all* three directions is consistent with a Dirac conelike dispersion centered at \mathbf{K}' .

In Fig. 5, we show constant energy slices through the magnon dispersion in the (H, K) plane at the energy transfers of $\hbar\omega^*$ and $\hbar\omega^* \pm 1$ meV. A generic constant energy slice through a 2D magnon dispersion (with fixed L) should yield high intensity along closed contours in the (H, K) plane. However, the constant energy slice at $\hbar\omega^*$ in Fig. 5(c) shows intensity maxima at only discrete *spots* located at the Dirac points. The observation of such discrete high-intensity momentum spots in a constant energy slice is highly unusual and is again a direct consequence of

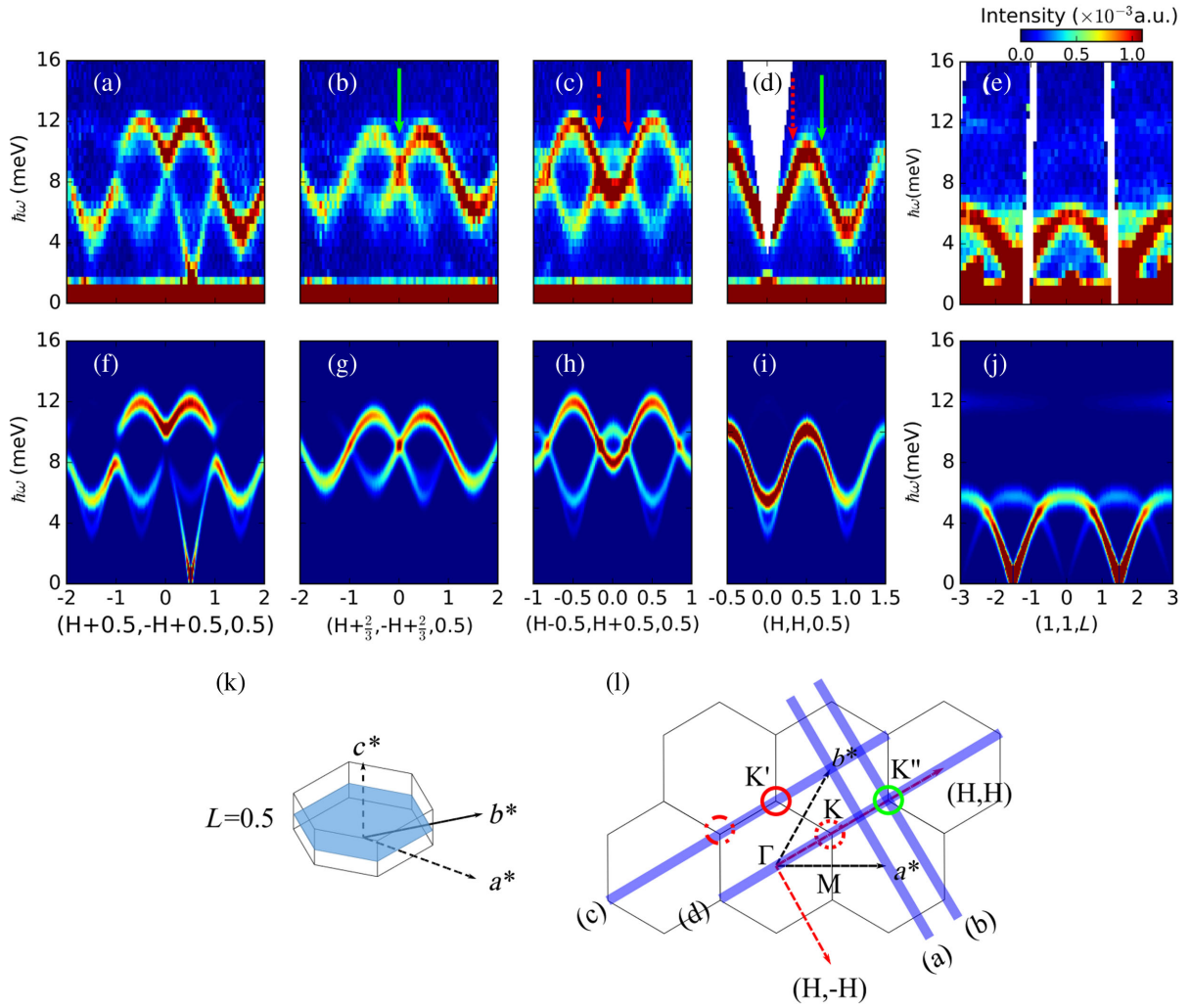


FIG. 3. (a)–(e) Momentum- and energy-resolved neutron scattering intensity map of magnons in CoTiO₃. The data were obtained at $T = 5$ K, with an incident neutron energy $E_i = 50$ meV at SEQUOIA at the Spallation Neutron Source (SNS). A pseudocolor intensity scale, where red (blue) denotes large (small) scattering intensity, is used to plot the data. Panels (a)–(d) show magnon excitations along $(H, -H)$ and (H, H) within the honeycomb plane at fixed $L = 0.5$, while panel (e) shows excitations along L for fixed in-plane momentum $(1, 1)$. (f)–(j) Calculated magnon spectra using $J_{\parallel,1} = -4.41$ meV, $J_{\perp,1} = 0$ meV, and $J_{\parallel,2'=2''} = J_{\perp,2'=2''} = 0.57$ meV after convolving with the experimental energy resolution of 1 meV using spinW [37]. (k) Schematics of the 3D BZ and (l) projection of 3D reciprocal space onto the 2D honeycomb plane. The $L = 0.5$ plane has been shaded in blue in panel (k). Directions of momentum transfers within the $L = 0.5$ plane in panels (a) to (d) are denoted by thick blue lines in panel (l). Circles in panel (l) indicate positions of the Dirac point where magnon bands cross, which are denoted by arrows in panels (b)–(d). Circles and arrows of the same line style and color are used for the same Dirac point.

the above-discussed conical dispersion near a Dirac magnon crossing point.

Below and above $\hbar\omega^*$, a constant energy slice through a Dirac cone dispersion should show closed contours in momentum space, as illustrated by the red loops in the theory plot in Fig. 5(b) (which we discuss further in the next section). However, the finite energy resolution, and the highly momentum-dependent dynamical structure factor (as these contours traverse different BZs), leads to strong intensity suppression along parts of the contour. This intensity asymmetry at fixed energy is already visible in

Figs. 4(a)–4(c). This asymmetry is most dramatic for magnon spectra along $(H + \frac{2}{3}, -H + \frac{2}{3}, 0.5)$ [Fig. 3(b)] and $(H, H, 0.5)$ [Fig. 3(d)]. These two orthogonal directions intersect at the Dirac point \mathbf{K}'' marked by a green circle in Fig. 5(d) [and Fig. 3(l)]. Away from \mathbf{K}'' (highlighted by a green arrow), Fig. 3(b) shows two magnon modes along $(H + \frac{2}{3}, -H + \frac{2}{3}, 0.5)$. Strikingly, only one of them is visible along the perpendicular direction shown in Fig. 3(d), while the intensity of the other mode is suppressed due to the small dynamical structure factor. However, the existence of two magnon modes along this direction is evident from

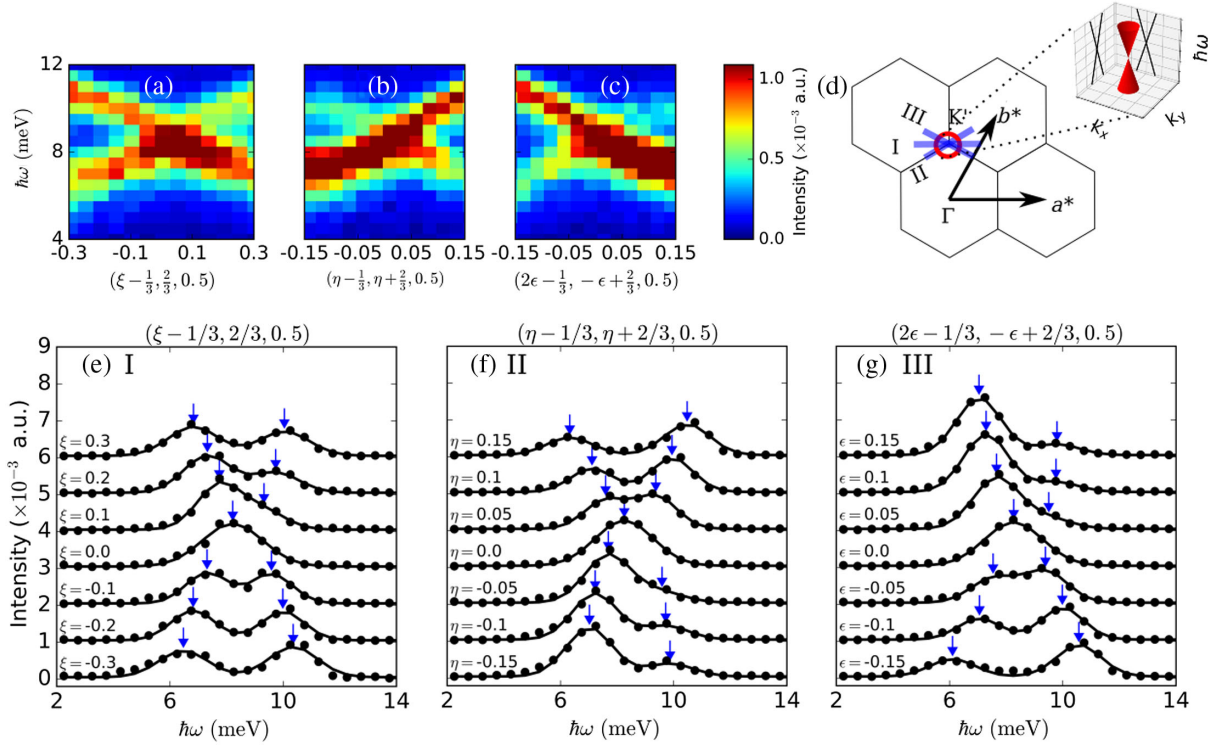


FIG. 4. (a)–(c) Magnon spectra close to $\mathbf{K}' = (-\frac{1}{3}, \frac{2}{3})$ along different momentum cuts indicated in panel (d), which lie in the (H, K) plane (with $L = 0.5$): (I) $(\xi - \frac{1}{3}, \frac{2}{3})$, (II) $(\eta - \frac{1}{3}, \eta + \frac{2}{3})$, and (III) $(2\epsilon - \frac{1}{3}, -\epsilon + \frac{2}{3})$. (d) BZ in the (H, K) plane, with the directions of I–III indicated by thick blue bars. The Dirac point \mathbf{K}' is denoted by a red circle [same as in Fig. 3(I)]. The Dirac cone near \mathbf{K}' is shown schematically in the inset. Cuts through different directions, which all pass through the Dirac point, should show an X-shaped dispersion (black solid line) where the magnon modes cross only at the Dirac point. (e)–(g) Measured intensity versus energy at fixed momentum along I–III, extracted from the magnon spectra in panels (a)–(c), respectively. The plots at different momenta in the same panel have been offset for clarity. Each cut is fit to two Gaussians with the same widths on top of a fixed constant background. Peak positions obtained from the fit are indicated by blue arrows.

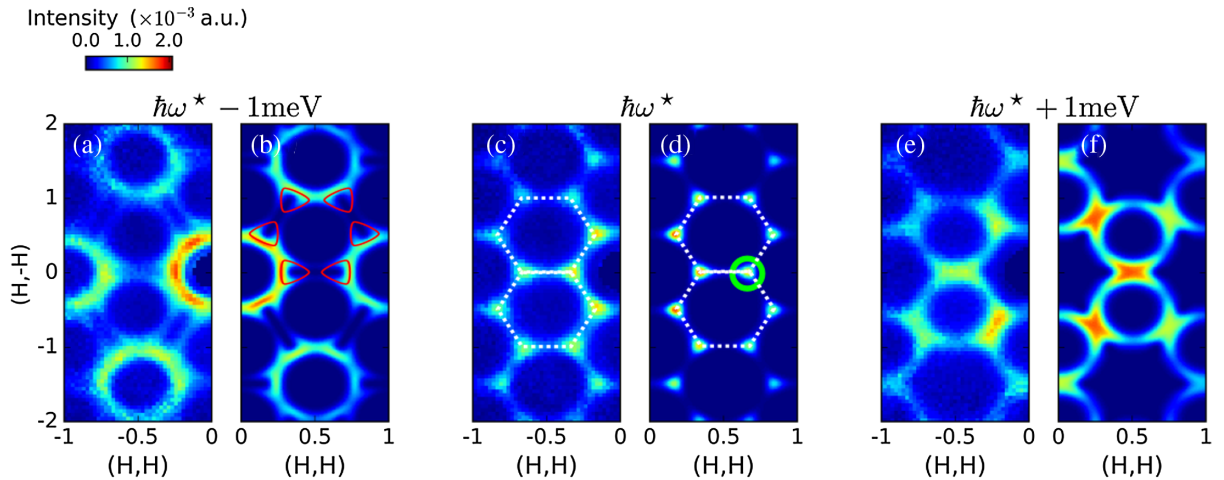


FIG. 5. (a,c,e) Constant energy slices of the CoTiO₃ magnon spectra in the (H, K) plane. The constant energy of each slice is chosen to be at the Dirac point crossing with $\hbar\omega^* \sim 8.5$ meV (c), 1 meV below $\hbar\omega^*$ (a), and 1 meV above $\hbar\omega^*$ (e). Since magnon spectra in CoTiO₃ have almost no L dependence at energies close to $\hbar\omega^*$, all spectra have been integrated over all L measured to improve statistics. (b,d,f) Calculated intensity maps using the same parameters as in Fig. 3. The calculated spectra are convolved with an energy resolution of 1 meV. An energy integration range of 0.5 meV has been used for both the experimental data and calculation. White dashed lines in panels (c) and (d) denote the boundaries of 2D BZs. Red triangles in panel (b) are loops in a constant energy slice of the magnon dispersion below the Dirac points. As in Fig. 3(I), the green circle in panel (d) indicates the position of the Dirac point \mathbf{K}'' .

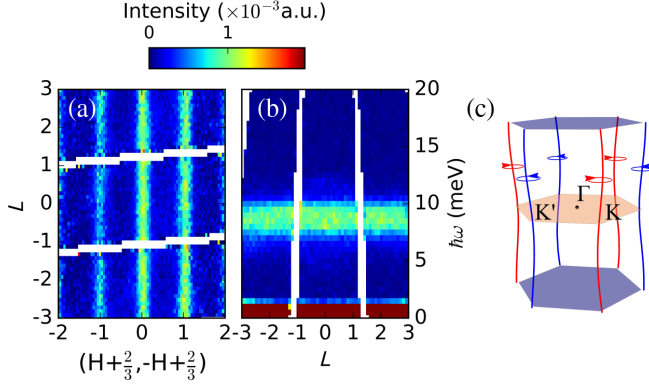


FIG. 6. (a) Slice of CoTiO₃ magnon spectra in the $(H + \frac{2}{3}, -H + \frac{2}{3}, L)$ plane at the Dirac energy $\hbar\omega^*$. (b) Magnon dispersion along L with fixed $H = K = \frac{2}{3}$. (c) Schematic plot of Dirac nodal lines in the 3D BZ winding near the corners with additional nearest-neighbor interplane antiferromagnetic couplings $J_{\parallel,3} > 0$ and $J_{\perp,3} < J_{\parallel,3}$. Arrows depict the vorticity associated with the nontrivial Berry phase winding characterizing the nodal lines (positive is shown in blue; negative is shown in red). See text and Supplemental Material [31] for details.

Fig. 3(c), which is completely equivalent to Fig. 3(d) up to an integer reciprocal lattice vector.

As we show next, the observed anisotropic distribution of magnon intensity is well reproduced by our calculations. Remarkably, our data suggest that the Dirac points in the (H, K) plane at different L appear to merge into a nodal line in the full 3D BZ [Fig. 6(a)], with no discernible dispersion along L [Fig. 6(b)].

IV. MODEL HAMILTONIAN

To understand the magnetic excitations in CoTiO₃, we carry out linear spin-wave calculations using a minimal model containing only nearest-neighbor (NN) intraplane and next-nearest-neighbor (NNN) interplane coupling labeled as 1, 2', and 2'' in Fig. 1(b). The magnitudes of interactions along 2' and 2'' are set to be the same due to similar exchange-path geometries. Using Δ_{trig} and λ determined for CoTiO₃, the magnetic interactions between the \tilde{S} pseudospins are expected to have strong easy-plane anisotropy (see Supplemental Material [31]). Interactions between the pseudospins are therefore taken to be of the XXZ type, given by $J_{\parallel}(\tilde{S}_{x,i}\tilde{S}_{x,j} + \tilde{S}_{y,i}\tilde{S}_{y,j}) + J_{\perp}\tilde{S}_{z,i}\tilde{S}_{z,j}$.

The neutron data shown in Figs. 3 and 5 are described very well by this simple model Hamiltonian with just two parameters: a ferromagnetic XY exchange coupling along bond 1 shown in Fig. 1(b) [$J_{\parallel,1} = -4.4(9)$ meV and $J_{\perp,1} = 0$ meV] and a Heisenberg antiferromagnetic exchange interaction on bonds 2' and 2'' [$J_{\parallel,2'=2''} = J_{\perp,2'=2''} = 0.6(1)$ meV]. We note that the fitting results are not changed by adding a small NN interplane coupling ($\lesssim 1$ meV), which connects two Co²⁺ directly on top of

each other along the c axis. The effect of such a NN interplane coupling on the magnon dispersion is likely to be negligible compared to the 2' and 2'' interactions because each spin has only one out-of-plane NN but nine NNN's. To compare our calculation directly with the data, we calculate the magnetic inelastic intensity using the expression $I(\mathbf{Q}, \omega) \propto \frac{1}{2}g_{\parallel}^2\mathcal{S}_{\parallel} + g_{\perp}^2\mathcal{S}_{\perp}$, where \mathcal{S}_{\parallel} (\mathcal{S}_{\perp}) denotes the in-plane (out-of-plane) fluctuations of pseudospins. (See Supplemental Material [31] for the derivation of this expression and further fitting details). The calculated magnon spectra are shown in Figs. 3(f)–3(j). Our results give four magnon modes due to the presence of four spins in a primitive unit cell. The scattering intensity of CoTiO₃ mostly comes from the two modes contributing to \mathcal{S}_{\parallel} because of the larger g_{\parallel} , as well as stronger in-plane spin fluctuations. As shown in Fig. 3(j), the dominant \mathcal{S}_{\parallel} contribution in our strongly XY model follows an $L = 3$ periodicity along L . A much weaker \mathcal{S}_{\perp} is displaced by $L = 1.5$ with respect to \mathcal{S}_{\parallel} . This result is entirely consistent with our data shown in Fig. 3(e) and allows us to rule out a simple Heisenberg model (see Supplemental Material [31]). The weak magnon intensity due to \mathcal{S}_{\perp} can also be identified in the data in Fig. 3(a), in further support of our effective spin model. Since the relative intensity of two transverse fluctuations \mathcal{S}_{\parallel} and \mathcal{S}_{\perp} is directly related to the exchange anisotropy J_{\perp}/J_{\parallel} , this ratio could be determined more precisely in future polarized inelastic neutron scattering experiments that can separately resolve the in-plane and out-of-plane spin fluctuations.

The calculated magnon spectra in Figs. 3(g) and 3(h) clearly show crossings of magnon modes at the Dirac points, which is consistent with results shown in Figs. 3(b) and 3(c). Constant energy slices, in the vicinity of $\hbar\omega^*$, are determined from our model [Figs. 5(b), 5(d), and 5(f)]. These results are in good agreement with Figs. 5(a), 5(c), and 5(e), taking into account finite energy resolution, in addition to the magnon dynamical structure factor. In particular, the triangular loops in the constant energy slice below $\hbar\omega^*$ resemble two lines connecting bigger rings [Fig. 5(b)], in excellent agreement with our data in Fig. 5(a).

Moreover, our model reproduces the observed merging of the 2D Dirac magnons at fixed L , seen at the 2D BZ corners in the (H, K) plane, into a full Dirac nodal line (DNL) along the L direction in the 3D BZ. The nodal line observed in CoTiO₃ is a magnon analogue of the DNL in 3D semimetals [6] or the symmetry-protected line degeneracy of 3D electronic bands. Similar to DNLs in 3D electronic materials without SOC, the XXZ spin model for CoTiO₃ features a topological Berry phase winding, which ensures its stability as observed in our data even when perturbations such as small changes of the exchange anisotropy, J_{\perp}/J_{\parallel} , or weak further-neighbor interactions are included (see Supplemental Material [31] for further

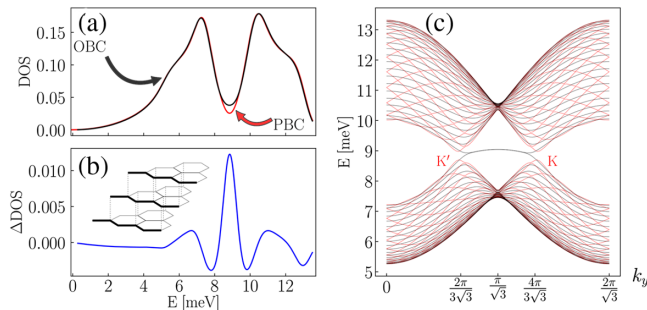


FIG. 7. (a) Calculated magnon density of states (DOS) for open boundary conditions (OBC, black) and periodic boundary conditions (PBC, red). The open boundary terminates on a surface with a zigzag edge. The DOS in both cases exhibits a V-shaped wedge arising from the bulk Dirac nodal lines. For OBC, the DOS is a sum of the surface and bulk magnon contributions. (b) The excess DOS, denoted Δ DOS, corresponds to the difference DOS (OBC)-DOS(PBC), and it arises from surface magnons appearing at the Dirac line node energy. The geometry of the zigzag edge of an ABC stacked honeycomb lattice is shown in the inset. (c) Magnon spectra along a cut parallel to the zigzag edge, k_y . Edge states can be seen connecting the bulk Dirac nodes at the Dirac energy $E \simeq 8.5$ meV. These states are responsible for the excess Δ DOS in panel (b). These surface magnon states are not found for a surface along the armchair edge (see Supplemental Material [31]).

discussion). In the presence of significant nearest-neighbor interplane XXZ exchange (denoted by J_3), the DNL is no longer pinned at \mathbf{K} for an arbitrary L but starts to spiral around it [see Fig. 6(c)]. Within our momentum resolution, we could not resolve any deviation of the DNL away from the \mathbf{K} points, which justifies the assumption of ignoring further-neighbor interactions in our theoretical model. Furthermore, given the in-plane magnetic order, the impact of the SOC-induced Dzyaloshinskii-Moriya interaction also vanishes at this high symmetry point by virtue of C_3 symmetry. Since relative magnitudes between magnetic interactions can be tuned by changing the lattice structure, one might be able to drive a systematic movement of the DNL in CoTiO_3 with pressure. Such DNLs may also be found in other ilmenite magnets, e.g., FeTiO_3 [38]; however, the location of DNLs might vary depending on their anisotropies [39].

The nontrivial topological Berry phase carried by the DNLs in CoTiO_3 also implies the existence of symmetry-protected surface states [14,40,41]. In CoTiO_3 , the DNLs form simple straight lines along L . This simple geometry of the DNLs guarantees that the surface magnons are found on side surfaces containing zigzag edges. This result is confirmed by our calculation of the magnon density of states (DOS), shown in Fig. 7(a), where we compare the DOS for periodic boundary conditions (PBC, red) with the DOS for open boundary conditions, which generates such a surface (OBC, black). In both plots, the overall V-shaped DOS with a dip near $E \approx 8.5$ meV is a clear indication

of a bulk DNL. However, the difference DOS, plotted in Fig. 7(b), exhibits a clear peak, with an excess DOS at precisely the Dirac node energy. From Fig. 7(c), we correlate this peak in the difference DOS with the presence of surface magnons in this geometry, by examining the magnon dispersion along the k_y direction in the surface BZ, where we find an extra surface magnon band running between two Dirac points for OBC, which is absent for PBC. Such surface magnon modes are not found on the surface containing the armchair edge or on the honeycomb surfaces (see Supplemental Material [31]). The observation that this excess DOS is only found on specific surface terminations, as well as the ability of obtaining large CoTiO_3 single crystals, which could be cut along different surfaces, makes it a unique example whose surface DOS can be directly measured by comparing the response from different surfaces. For instance, Raman scattering, which is more surface sensitive than neutron scattering, could be used to test for these surface states. Raman scattering, which creates magnon pairs with opposite momenta $(\mathbf{q}, -\mathbf{q})$, can effectively probe the two-magnon DOS at the zone center $N(E) = \sum_{\mathbf{q}} \delta(\omega(\mathbf{q}) + \omega(-\mathbf{q}) - E)$. However, since $\omega(\mathbf{q}) = \omega(-\mathbf{q})$ due to the inversion symmetry of CoTiO_3 , this will be proportional to the single magnon DOS at energy $E/2$ as determined from Fig. 7. With improved energy resolution, resonant inelastic x-ray scattering (RIXS) could also be used to detect these surface magnons. To differentiate between bulk and surface magnons, scattering geometry in the RIXS experiment could be varied between grazing and normal incidence, which are more sensitive to scattering by the surface and bulk, respectively. In addition, since the excess DOS is found exclusively on a zigzag edge in CoTiO_3 , Raman or RIXS spectra on the honeycomb or armchair surfaces can be used as a bulk signal background and subtracted from that of a zigzag surface to isolate the contribution due to surface magnons.

V. BEYOND THE XXZ MODEL

One important observation that is not captured by our XXZ model is the existence of a small magnetic anisotropy within the honeycomb plane. This anisotropy is inferred from the highly nonlinear magnetization at $T = 5$ K for in-plane fields 1–4 Tesla, with a peak susceptibility at about 2 Tesla, which is likely a result of rotation of magnetic domains [42]. An in-plane anisotropy also implies the existence of a small gap at the magnetic zone center in the magnon dispersion. Although our experimental resolution does not allow us to determine the gap size directly, extrapolation of the magnon dispersion in Fig. 3(a) suggests a gap of order about 1 meV (see Supplemental Material [31]). Such a gap in the Goldstone mode can arise from bond-anisotropic exchange couplings, like the Kitaev interaction, due to quantum order by disorder, which pins the order parameter to the crystal axes. A phenomenological way to account for this is via a

pinning field $(-1)^z g_{\parallel} \mu_B h \tilde{S}_x$, staggered from layer to layer, deep in the ordered phase. We find that incorporating a pinning field of about 2 Tesla, based on the magnetization data, leads to a zone center gap of about 1 meV in the magnon dispersion, consistent with the above INS estimate. Remarkably, the Hamiltonian including such a pinning field continues to support a DNL near the \mathbf{K} points. A complete theoretical study of such weak bond-anisotropic exchanges will be discussed in a separate publication [43].

VI. CONCLUSION

We have carried out inelastic neutron scattering on quantum antiferromagnet CoTiO_3 with an ilmenite structure. The magnetic excitations in CoTiO_3 are well described using a simple model with dominant XY interactions. Our data show evidence for magnon crossings along a one-dimensional DNL in this material. In the vicinity of the DNL, magnons have a Dirac cone dispersion, which is analogous to ABC stacked graphene. This case is to be contrasted with the only other Dirac magnon candidate, Cu_3TeO_6 [20,22], which shows magnon crossing at (zero-dimensional) Dirac points. We showed that the simple magnon Hamiltonian of CoTiO_3 gives rise to magnon surface states only on certain surfaces. Such surface states can be readily probed in future experiments because two types of surface cut along different crystallographic orientations could be prepared easily with large single crystals of CoTiO_3 .

Our findings also establish CoTiO_3 as a candidate model system for studying transitions into other topological phases such as 3D Weyl magnons [44] and magnon topological insulators [13] under external perturbations. The ease of chemical substitution on both Co and Ti sites and the ability to grow large high-quality CoTiO_3 single crystals with high mechanical strength make it an ideal material for future studies of the impact of doping, hydrostatic pressure, strain, and magnetic fields, on gapless Dirac magnons. In addition, ilmenites can be grown as epitaxial thin films using conventional oxide film growth methods [45], which enables one to study surface states under epitaxial strain or to incorporate them into spintronics devices.

The close resemblance between CoTiO_3 and graphene allows a direct comparison between bosonic and fermionic responses to external perturbations. For example, the Dirac magnons in CoTiO_3 serve as an ideal model system for studying emergent gauge fields through strain engineering [24] or renormalization of the magnon bands resulting from the interparticle interaction between Dirac bosons [14,46]. Finally, unlike a simple Heisenberg ferromagnet, for which the electronic analogue is a simple tight-binding hopping Hamiltonian, the full model Hamiltonian for CoTiO_3 contains pairing terms analogous to the Bogoliubov–Gennes Hamiltonian [6] of a superconductor. Such

unconventional superconducting phases on the layered honeycomb lattice have begun to garner great attention due to the recent discovery of superconductivity in “magic angle” twisted bilayer graphene [47], providing further impetus to explore such remarkable analogies between electronic quasiparticles and bosonic magnons.

ACKNOWLEDGMENTS

Work at the University of Toronto was supported by the Natural Science and Engineering Research Council (NSERC) of Canada. F. C. C. acknowledges funding support from the Ministry of Science and Technology (MOST) in Taiwan under Projects No. 106-2119-M-002-035-MY3 and No. 108-2622-8-002-016, AI-MAT Project No. 108L900903 from the Ministry of Education in Taiwan, and Academia Sinica (AS-iMATE-108-11). G. J. S. acknowledges the support provided by MOST-Taiwan under Project No. 108-2112-M-027-002-MY3. This research used resources at the Spallation Neutron Source, a DOE Office of Science User Facility operated by the Oak Ridge National Laboratory. Use of the MAD beamline at the McMaster Nuclear Reactor is supported by McMaster University and the Canada Foundation for Innovation.

-
- [1] K. S. Novoselov, A. K. Geim, S. V. Morozov, D. Jiang, M. I. Katsnelson, I. V. Grigorieva, S. V. Dubonos, and A. A. Firsov, *Two-Dimensional Gas of Massless Dirac Fermions in Graphene*, *Nature (London)* **438**, 197 (2005).
 - [2] Y. Zhang, Y.-W. Tan, H. L. Stormer, and P. Kim, *Experimental Observation of the Quantum Hall Effect and Berry’s Phase in Graphene*, *Nature (London)* **438**, 201 (2005).
 - [3] M. I. Katsnelson, K. S. Novoselov, and A. K. Geim, *Chiral Tunnelling and the Klein Paradox in Graphene*, *Nat. Phys.* **2**, 620 (2006).
 - [4] A. H. C. Neto, F. Guinea, N. M. R. Peres, K. S. Novoselov, and A. K. Geim, *The Electronic Properties of Graphene*, *Rev. Mod. Phys.* **81**, 109 (2009).
 - [5] T. O. Wehling, A. M. Black-Schaffer, and A. V. Balatsky, *Dirac Materials*, *Adv. Phys.* **63**, 1 (2014).
 - [6] C.-K. Chiu, J. C. Y. Teo, A. P. Schnyder, and S. Ryu, *Classification of Topological Quantum Matter with Symmetries*, *Rev. Mod. Phys.* **88**, 035005 (2016).
 - [7] L. Lu, J. D. Joannopoulos, and M. Soljacic, *Topological Photonics*, *Nat. Photonics* **8**, 821 (2014).
 - [8] T. Ozawa, H. M. Price, A. Amo, N. Goldman, M. Hafezi, L. Lu, M. C. Rechtsman, D. Schuster, J. Simon, O. Zilberberg, and I. Carusotto, *Topological Photonics*, *Rev. Mod. Phys.* **91**, 015006 (2019).
 - [9] Y. Jin, R. Wang, and H. Xu, *Recipe for Dirac Phonon States with a Quantized Valley Berry Phase in Two-Dimensional Hexagonal Lattices*, *Nano Lett.* **18**, 7755 (2018).
 - [10] T. Zhang, Z. Song, A. Alexandradinata, H. Weng, C. Fang, L. Lu, and Z. Fang, *Double-Weyl Phonons in Transition-Metal Monosilicides*, *Phys. Rev. Lett.* **120**, 016401 (2018).

- [11] H. Miao, T. T. Zhang, L. Wang, D. Meyers, A. H. Said, Y. L. Wang, Y. G. Shi, H. M. Weng, Z. Fang, and M. P. M. Dean, *Observation of Double Weyl Phonons in Parity-Breaking FeSi*, *Phys. Rev. Lett.* **121**, 035302 (2018).
- [12] J. Fransson, A. M. Black-Schaffer, and A. V. Balatsky, *Magnon Dirac Materials*, *Phys. Rev. B* **94**, 075401 (2016).
- [13] S. Owerre, *A First Theoretical Realization of Honeycomb Topological Magnon Insulator*, *J. Phys. Condens. Matter* **28**, 386001 (2016).
- [14] S. S. Pershoguba, S. Banerjee, J. C. Lashley, J. Park, H. Ågren, G. Aeppli, and A. V. Balatsky, *Dirac Magnons in Honeycomb Ferromagnets*, *Phys. Rev. X* **8**, 011010 (2018).
- [15] D. Boyko, A. V. Balatsky, and J. T. Haraldsen, *Evolution of Magnetic Dirac Bosons in a Honeycomb Lattice*, *Phys. Rev. B* **97**, 014433 (2018).
- [16] L. Zhang, J. Ren, J.-S. Wang, and B. Li, *Topological Magnon Insulator in Insulating Ferromagnet*, *Phys. Rev. B* **87**, 144101 (2013).
- [17] A. Mook, J. Henk, and I. Mertig, *Edge States in Topological Magnon Insulators*, *Phys. Rev. B* **90**, 024412 (2014).
- [18] R. Chisnell, J. S. Helton, D. E. Freedman, D. K. Singh, R. I. Bewley, D. G. Nocera, and Y. S. Lee, *Topological Magnon Bands in a Kagome Lattice Ferromagnet*, *Phys. Rev. Lett.* **115**, 147201 (2015).
- [19] L. Chen, J.-H. Chung, B. Gao, T. Chen, M. B. Stone, A. I. Kolesnikov, Q. Huang, and P. Dai, *Topological Spin Excitations in Honeycomb Ferromagnet CrI₃*, *Phys. Rev. X* **8**, 041028 (2018).
- [20] W. Yao, C. Li, L. Wang, S. Xue, Y. Dan, K. Iida, K. Kamazawa, K. Li, C. Fang, and Y. Li, *Topological Spin Excitations in a Three-Dimensional Antiferromagnet*, *Nat. Phys.* **14**, 1011 (2018).
- [21] F. Lu and Y.-M. Lu, *Magnon Band Topology in Spin-Orbital Coupled Magnets: Classification and Application to α -RuCl₃*, [arXiv:1807.05232](https://arxiv.org/abs/1807.05232).
- [22] S. Bao, J. Wang, W. Wang, . Cai, S. Li, Z. Ma, D. Wang, K. Ran, Z.-Y. Dong, D. L. Abernathy, S.-L. Yu, X. Wan, J.-X. Li, and J. Wen, *Discovery of Coexisting Dirac and Triply Degenerate Magnons in a Three-Dimensional Antiferromagnet*, *Nat. Commun.* **9**, 2591 (2018).
- [23] V. M. Pereira, J. M. B. L. dos Santos, and A. H. C. Neto, *Modeling Disorder in Graphene*, *Phys. Rev. B* **77**, 115109 (2008).
- [24] F. Guinea, M. I. Katsnelson, and A. K. Geim, *Energy Gaps and a Zero-Field Quantum Hall Effect in Graphene by Strain Engineering*, *Nat. Phys.* **6**, 30 (2010).
- [25] V. M. Pereira and A. H. C. Neto, *Strain Engineering of Graphene's Electronic Structure*, *Phys. Rev. Lett.* **103**, 046801 (2009).
- [26] S. Y. Zhou, G.-H. Gweon, A. V. Fedorov, P. N. First, W. A. de Heer, D.-H. Lee, F. Guinea, A. H. C. Neto, and A. Lanzara, *Substrate-Induced Bandgap Opening in Epitaxial Graphene*, *Nat. Mater.* **6**, 770 (2007).
- [27] S. Y. Zhou, D. A. Siegel, A. V. Fedorov, and A. Lanzara, *Metal to Insulator Transition in Epitaxial Graphene Induced by Molecular Doping*, *Phys. Rev. Lett.* **101**, 086402 (2008).
- [28] J.-H. Chen, W. G. Cullen, C. Jang, M. S. Fuhrer, and E. D. Williams, *Defect Scattering in Graphene*, *Phys. Rev. Lett.* **102**, 236805 (2009).
- [29] M. O. Goerbig, *Electronic Properties of Graphene in a Strong Magnetic Field*, *Rev. Mod. Phys.* **83**, 1193 (2011).
- [30] R. E. Newnham, J. H. Fang, and R. P. Santoro, *Crystal Structure and Magnetic Properties of CoTiO₃*, *Acta Cryst.* **17**, 240 (1964).
- [31] See Supplemental Material at <http://link.aps.org/supplemental/10.1103/PhysRevX.10.011062> for details of experimental methods, theoretical modelling, and Supplemental figures.
- [32] K. A. Ross, J. M. Brown, R. J. Cava, J. W. Krizan, S. E. Nagler, J. A. Rodriguez-Rivera, and M. B. Stone, *Single-Ion Properties of the $S_{\text{eff}} = \frac{1}{2}$ XY Antiferromagnetic Pyrochlores NaA'Co₂F₇ (A' = Ca²⁺, Sr²⁺)*, *Phys. Rev. B* **95**, 144414 (2017).
- [33] W. J. L. Buyers, T. M. Holden, E. C. Svensson, R. A. Cowley, and M. T. Hutchings, *Excitations in KCoF₃. II. Theoretical*, *J. Phys. C* **4**, 2139 (1971).
- [34] H. Liu and G. Khaliullin, *Pseudospin Exchange Interactions in d^7 Cobalt Compounds: Possible Realization of the Kitaev Model*, *Phys. Rev. B* **97**, 014407 (2018).
- [35] R. Sano, Y. Kato, and Y. Motome, *Kitaev-Heisenberg Hamiltonian for High-Spin d^7 Mott Insulators*, *Phys. Rev. B* **97**, 014408 (2018).
- [36] H. Watanabe, H. Yamauchi, and H. Takei, *Magnetic Anisotropies in MTiO₃ (M = Co, Ni)*, *J. Magn. Magn. Mater.* **15–18**, 549 (1980).
- [37] S. Toth and B. Lake, *Linear Spin Wave Theory for Single-Q Incommensurate Magnetic Structures*, *J. Phys. Condens. Matter* **27**, 166002 (2015).
- [38] H. Kato, Y. Yamaguchi, M. Yamada, S. Funahashi, Y. Nakagawa, and H. Takei, *Neutron Scattering Study of Magnetic Excitations in Oblique Easy-Axis Antiferromagnet FeTiO₃*, *J. Phys. C* **19**, 6993 (1986).
- [39] J. B. Goodenough and J. J. Stickler, *Theory of the Magnetic Properties of the Ilmenites MTiO₃*, *Phys. Rev.* **164**, 768 (1967).
- [40] T. Hyart, R. Ojajarvi, and T. T. Heikkilä, *Two Topologically Distinct Dirac-Line Semimetal Phases and Topological Phase Transitions in Rhombohedrally Stacked Honeycomb Lattices*, *J. Low Temp. Phys.* **191**, 35 (2018).
- [41] Q. Xie, J. Li, M. Liu, L. Wang, D. Li, Y. Li, and X.-Q. Chen, *Phononic Weyl Nodal Straight Lines in High-Temperature Superconductor MgB₂*, *Phys. Rev. B* **101**, 045403 (2020).
- [42] A. M. Balbashov, A. A. Mukhin, V. Yu. Ivanov, L. D. Iskhakova, and M. E. Voronchikhina, *Electric and Magnetic Properties of Titanium-Cobalt-Oxide Single Crystals Produced by Floating Zone Melting with Light Heating*, *Low Temp. Phys.* **43**, 965 (2017).
- [43] I. Khait, B. Yuan, Y.-J. Kim, and A. Paramekanti (to be published).
- [44] F.-Y. Li, Y.-D. Li, Y. B. Kim, L. Balents, Y. Yu, and G. Chen, *Weyl Magnons in Breathing Pyrochlore Antiferromagnets*, *Nat. Commun.* **7**, 12691 (2016).

- [45] T. Varga, T. C. Droubay, M. E. Bowden, P. Nachimuthu, V. Shutthanandan, T. B. Bolin, W. A. Shelton, and S. A. Chambers, *Epitaxial Growth of NiTiO₃ with a Distorted Ilmenite Structure*, *Thin Solid Films* **520**, 5534 (2012).
- [46] W. B. Yelon and R. Silbergliitt, *Renormalization of Large-Wave-Vector Magnons in Ferromagnetic CrBr₃ Studied by Inelastic Neutron Scattering: Spin-Wave Correlation Effects*, *Phys. Rev. B* **4**, 2280 (1971).
- [47] Y. Cao, V. Fatemi, S. Fang, K. Watanabe, T. Taniguchi, E. Kaxiras, and P. J. Herrero, *Unconventional Superconductivity in Magic-Angle Graphene Superlattices*, *Nature (London)* **556**, 43 (2018).